J. Fluid Mech. (1999), *vol.* 391, *pp.* 189–209. Printed in the United Kingdom

© 1999 Cambridge University Press

Impulse formulation of the Euler equations: general properties and numerical methods

By GIOVANNI RUSSO[1] AND PETER SMEREKA[2]

[1]Dipartimento di Matematica Pura ed Applicata, Università dell'Aquila, Via Vetoio, 67010 L'Aquila, Italy

[2]Department of Mathematics, University of Michigan, Ann Arbor, MI 48109, USA

(Received 26 June 1997 and in revised form 26 January 1999)

The gauge freedom of the incompressible Euler equations is explored. We present various forms of the Euler equations written in terms of the impulse density. It is shown that these various forms are related by a gauge transformation. We devise a numerical method to solve the impulse form of the Euler equations in a variety of gauges. The numerical scheme is implemented both in two and three space dimensions. Numerical results are presented showing that the impulse density tends to concentrate on sheets.

1. Introduction

Incompressible Euler and Navier–Stokes equations can be written in terms of a vector field, $\boldsymbol{p}$, that has the property that the fluid velocity, $\boldsymbol{u}$, is the divergence-free projection of $\boldsymbol{p}$. Several choices are possible for $\boldsymbol{p}$, which describe the same fluid motion. The different choices depend on a gauge transformation. According to each particular gauge, an evolution equation for $\boldsymbol{p}$ describes the motion of the fluid.

In recent years there has been a growing interest in this formulation of incompressible fluid dynamics although the consequences of the gauge invariance and the properties of the solution of the variable $\boldsymbol{p}$ have not yet been fully analysed. In a particular gauge, the vector field $\boldsymbol{p}$ has an interesting geometrical meaning: it describes the evolution of material surfaces; its direction is orthogonal to the material surface element, and its length is proportional to the area of the surface element. This issue has been explored by Sagdeev *et al.* (1982) and Tur & Yanovsky (1993). In this same gauge, Oseledets (1989) and Kuz'min (1983) have shown that the evolution equation for the fluid has a Hamiltonian structure. Lagrangian numerical methods based on this Hamiltonian formulation have been developed for initial value problems by Buttke (1993, see also Buttke & Chorin 1993). E & Liu (1997) have developed Eulerian numerical methods to solve this impulse equation. Cortez (1996) and Recchioni & Russo (1998) have developed Lagrangian methods in the impulse variable to study the motion of membrane in an inviscid fluid. Chorin (1994) has used this formulation to study models of turbulence.

Maddocks & Pego (1995) have exploited the gauge freedom to generalize the impulse equation and present an unconstrained Hamiltonian formulation in terms of what they call the 'impetus'. Smereka (1996) has also used the gauge freedom to develop alternative forms of the impulse equation, one of which is used to develop a model of uniform turbulence. E & Liu (1998) have used yet another gauge to develop numerical methods for solving the incompressible Navier–Stokes equation.

https://doi.org/10.1017/S0022112099005170 Published online by Cambridge University Press

Given the wide interest in this formulation, it would seem useful to have a method for the numerical solution of the impulse equation. One approach is to implement a numerical scheme directly based on the impulse equation; such a method would simultaneously yield the velocity field as well. Unfortunately, straightforward implementations of such schemes do not work well because the impulse equation is only weakly well posed (Chen, 1996; E & Liu 1997). E & Liu (1997) went on to provide a numerical method which alleviated this difficulty in one particular gauge.

In this paper we provide three new methods which also ameliorate the difficulties associated with the problem being weakly well posed. The main idea behind these methods is to first solve the incompressible Euler equations using a standard projection scheme, then a separate equation is solved for the impulse density. In this way the computation of the impulse does not affect the fluid velocity. Furthermore the equation we solve for the impulse density appears to be well posed.

We stress that the purpose of this paper is *not* to present a new method for solving the incompressible Euler equations but rather to present methods for the computation of the impulse density. We believe that the impulse variable could be used as a diagnostic tool. In fact, as we have just mentioned, the impulse equation, in general, has no particular advantage in providing a solution of the incompressible Euler equations. On the other hand, E & Liu (1997) have proposed one particular impulse formulation which appears to be a promising alternative to the standard projection method.

The plan of the paper is the following: in the next section we describe the impulse formulation in different gauges, and we point out the physical and geometrical interpretation of these equations. In § 3 we show the difficulties associated with the direct numerical solution of the impulse equations, and we present the schemes for solving the impulse equations which are based on the numerical solution of the Euler equations. In § 4 we present numerical solutions of the impulse equations in two and three dimensions in a periodic domain.

2. Impulse formulation of the Euler equations

The Euler equations for an incompressible fluid with unit density are

$$\nabla \cdot \boldsymbol{u} = 0, \tag{2.1}$$

$$\frac{\partial \boldsymbol{u}}{\partial t} + \boldsymbol{u} \cdot \nabla \boldsymbol{u} = -\nabla \mathscr{P}, \tag{2.2}$$

where $\boldsymbol{u}$ is the fluid velocity, and $\mathscr{P}$ the pressure. Let us consider a vector field that has the same curl as the velocity:

$$\boldsymbol{p} = \boldsymbol{u} + \nabla \phi. \tag{2.3}$$

We shall call this vector field the *impulse density*. An interpretation of $\boldsymbol{p}$ is given by Smereka (1996).

Note that $\boldsymbol{p}$ is uniquely defined up to a gradient. The evolution equation for $\boldsymbol{p}$ is derived as follows. Equation (2.2) can be written as

$$\frac{\partial \boldsymbol{u}}{\partial t} - \boldsymbol{u} \times (\nabla \times \boldsymbol{u}) = -\nabla \left(\mathscr{P} + \tfrac{1}{2} \boldsymbol{u} \cdot \boldsymbol{u} \right). \tag{2.4}$$

We then substitute (2.3) into (2.4) to obtain

$$\frac{\partial \boldsymbol{p}}{\partial t} - \boldsymbol{u} \times (\nabla \times \boldsymbol{p}) = -\nabla \left(\mathscr{P} + \tfrac{1}{2} \boldsymbol{u} \cdot \boldsymbol{u} - \frac{\partial \phi}{\partial t} \right). \tag{2.5}$$

https://doi.org/10.1017/S0022112099005170 Published online by Cambridge University Press

Since ϕ is arbitrary, the above equation can be written as

$$\frac{\partial \boldsymbol{p}}{\partial t} - \boldsymbol{u} \times (\nabla \times \boldsymbol{p}) = \nabla \Lambda, \tag{2.6}$$

where Λ is an arbitrary scalar field which we shall call the *gauge*. Since $\boldsymbol{u}$ and $\boldsymbol{p}$ differ only by a gradient, then the velocity field, $\boldsymbol{u}$, is the divergence-free projection of $\boldsymbol{p}$. It is computed using (2.3) where ϕ satisfies

$$\Delta \phi = \nabla \cdot \boldsymbol{p}. \tag{2.7}$$

In a more compact form we may write

$$\boldsymbol{u} = \mathbf{P}\boldsymbol{p} = (\boldsymbol{I} - \nabla \Delta^{-1} \nabla \cdot)\boldsymbol{p}. \tag{2.8}$$

The choice of the gauge will determine the evolution equation for $\boldsymbol{p}$. If we choose

$$\Lambda = 0$$

we find

$$\frac{\partial \boldsymbol{p}}{\partial t} - \boldsymbol{u} \times (\nabla \times \boldsymbol{p}) = 0. \tag{2.9}$$

We shall call this the *zero gauge*. If we choose

$$\Lambda = -\boldsymbol{u} \cdot \boldsymbol{p} + \tfrac{1}{2} \boldsymbol{u} \cdot \boldsymbol{u}$$

we obtain the equation

$$\frac{\partial \boldsymbol{p}}{\partial t} + \boldsymbol{u} \cdot \nabla \boldsymbol{p} = -(\nabla \boldsymbol{u})^T \nabla \phi, \tag{2.10}$$

where ϕ is given by equation (2.7), which Maddocks & Pego (1995) derived by variational considerations. They called $\boldsymbol{p}$ the *impetus*. This will be called the *MP gauge*.

If we choose the gauge

$$\Lambda = -\tfrac{1}{2} \boldsymbol{u} \cdot \boldsymbol{u},$$

we obtain the equation

$$\frac{\partial \boldsymbol{p}}{\partial t} + \boldsymbol{u} \cdot \nabla \boldsymbol{u} = 0.$$

This gauge was introduced by E & Liu (1998) to develop numerical schemes for the incompressible Navier–Stokes equations. We shall call this gauge the *EL gauge*.

By choosing the gauge

$$\Lambda = -\boldsymbol{u} \cdot \boldsymbol{p}$$

we obtain

$$\frac{\partial \boldsymbol{p}}{\partial t} + \boldsymbol{u} \cdot \nabla \boldsymbol{p} = -(\nabla \boldsymbol{u})^T \boldsymbol{p}. \tag{2.11}$$

We shall call this the *geometric gauge*. This is probably the most popular impulse equation, and the one that has been more extensively studied. This is the gauge used by Buttke (1993), Buttke & Chorin (1993), Cortez (1996) and Recchioni & Russo (1998) in their numerical computations. Furthermore, Sagdeev *et al* (1982) and Tur & Yanovsky (1993) have used this gauge to investigate new topological invariants for ideal fluids. It is interesting to note that ϕ satisfies a partial differential equation. It follows from (2.5) and (2.6) that

$$\frac{\partial \phi}{\partial t} = \mathscr{P} + \tfrac{1}{2} \boldsymbol{u} \cdot \boldsymbol{u} + \Lambda. \tag{2.12}$$

https://doi.org/10.1017/S0022112099005170 Published online by Cambridge University Press

Equation (2.12), in the zero gauge, becomes

$$\frac{\partial \phi}{\partial t} = \mathscr{P} + \tfrac{1}{2}\boldsymbol{u}\cdot\boldsymbol{u}. \tag{2.13}$$

In the MP gauge we find

$$\frac{\partial \phi}{\partial t} + \boldsymbol{u}\cdot\nabla\phi = \mathscr{P}. \tag{2.14}$$

In the EL gauge it is

$$\frac{\partial \phi}{\partial t} = \mathscr{P}, \tag{2.15}$$

and in the geometric gauge one has

$$\frac{\partial \phi}{\partial t} + \boldsymbol{u}\cdot\nabla\phi = \mathscr{P} - \tfrac{1}{2}\boldsymbol{u}\cdot\boldsymbol{u}. \tag{2.16}$$

Finally, we remark that the choice $\Lambda = -\mathscr{P} - \frac{1}{2}\boldsymbol{u}\cdot\boldsymbol{u}$ and $\phi(\boldsymbol{x},0) = 0$ gives $\boldsymbol{p} = \boldsymbol{u}$, in other words $\boldsymbol{p}$ satisfies the usual Euler equations.

2.1. *Properties*

The following properties are true for all gauges:

(i) We observe that for a given flow on a fixed domain Ω, the value of $\boldsymbol{p}$ that has the minimal L^2 norm is obtained for $\boldsymbol{p} = \boldsymbol{u}$. To see this we note that

$$\|\boldsymbol{p}\|_2^2 = \int_\Omega |\boldsymbol{u} + \nabla\phi|^2 \,\mathrm{d}x.$$

Integrating by parts and observing that $\boldsymbol{u}\cdot\boldsymbol{n} = 0$ for $\boldsymbol{x} \in \partial\Omega$ we find

$$\|\boldsymbol{p}\|_2^2 = \int_\Omega \left(|\boldsymbol{u}|^2 + |\nabla\phi|^2\right) \,\mathrm{d}x \tag{2.17}$$

and the claim follows.

(ii) The Kelvin–Helmholtz circulation theorem states that

$$\frac{\mathrm{d}}{\mathrm{d}t}\oint \boldsymbol{u}\cdot\mathrm{d}\ell = 0.$$

Since $\boldsymbol{p} = \boldsymbol{u} + \nabla\phi$ then it follows that

$$\frac{\mathrm{d}}{\mathrm{d}t}\oint \boldsymbol{p}\cdot\mathrm{d}\ell = 0.$$

This was pointed out by Buttke (1993).

(iii) The impulse of a region of fluid, Ω, is given by (Batchelor 1967, § 7.2)

$$I = \frac{1}{2}\int_\Omega \boldsymbol{r}\times\boldsymbol{\omega}\mathrm{d}V. \tag{2.18}$$

Since $\boldsymbol{\omega} = \nabla\times\boldsymbol{p}$ then it follows after an integration by parts that

$$I = \int_\Omega \boldsymbol{p}\mathrm{d}V + \int_{\partial\Omega}\left[(\boldsymbol{r}\cdot\boldsymbol{p})\boldsymbol{n} - (\boldsymbol{r}\cdot\boldsymbol{n})\boldsymbol{p}\right]\mathrm{d}S. \tag{2.19}$$

If the support of $\boldsymbol{p}$ is Ω then (2.18) represents the total impulse of the fluid. Furthermore, as pointed out by Buttke (1993), if $\boldsymbol{\omega}$ has compact support (and if the kinetic

https://doi.org/10.1017/S0022112099005170 Published online by Cambridge University Press

energy of the fluid is finite in two dimensions), then it is possible to find $\boldsymbol{p}$ with compact support, and therefore (2.19) becomes

$$I = \int_{\Omega} \boldsymbol{p} \mathrm{d}V. \tag{2.20}$$

This equation shows that $\boldsymbol{p}$ can be thought of as the impulse density. Equation (2.20) can be found in Buttke (1993). The equation continues to be valid even if $\boldsymbol{p}$ does not have compact support, provided it decays fast enough at infinity. Next, we study properties of various gauges.

Zero gauge. The impulse equation in this gauge is rather interesting in that there are no stretching terms. We claim that (2.9) has the structure of a degenerate hyperbolic system. To see this we note that (2.9) can be written as

$$\frac{\partial p_\alpha}{\partial t} + A^{\gamma}_{\alpha\beta} \frac{\partial p_\beta}{\partial x_\gamma} = 0 \quad \text{where} \quad A^{\gamma}_{\alpha\beta} = \delta_{\beta\alpha} u_\gamma - \delta_{\alpha\gamma} u_\beta.$$

The above system is hyperbolic if for any direction $\boldsymbol{n}$ the matrix $\boldsymbol{A}^{\gamma}_{n_\gamma} = \boldsymbol{A}_n$ has three real eigenvalues with three independent eigenvectors. We find that

$$\boldsymbol{A}_n = \boldsymbol{u} \cdot \boldsymbol{n} \boldsymbol{I} - \boldsymbol{n} \otimes \boldsymbol{u}.$$

In component form

$$\boldsymbol{A}_n = \begin{pmatrix} u_2 n_2 + u_3 n_3 & -u_2 n_1 & -u_3 n_1 \\ -u_1 n_2 & u_1 n_1 + u_3 n_3 & -u_3 n_2 \\ -u_1 n_3 & -u_2 n_3 & u_1 n_1 + u_2 n_2 \end{pmatrix}.$$

The eigenvalues are $\lambda = \{0, \boldsymbol{u} \cdot \boldsymbol{n}, \boldsymbol{u} \cdot \boldsymbol{n}\}$. The eigenvector associated with $\lambda = 0$ is $\boldsymbol{n}$. The eigenspace, $R_\perp$, associated with $\lambda = \boldsymbol{u} \cdot \boldsymbol{n}$ is the space orthogonal to $\boldsymbol{u}$. If $\boldsymbol{u} \cdot \boldsymbol{n} \neq 0$ then R^3 is spanned by $\boldsymbol{n}$ and $R_\perp$, but if $\boldsymbol{u} \cdot \boldsymbol{n} = 0$ then the system does not have three independent eigenvectors. Consequently the system is a degenerate hyperbolic system.

It is interesting to observe that if the support of $\boldsymbol{p}$ is compact initially, it will remain compact for later times; however, because of the zero eigenvalue, the support of $\boldsymbol{p}$ is not carried with the fluid, but its size increases monotonically. It is true that

$$\Omega_t \subseteq \bigcup_{\tau=0}^{t} A_\tau$$

where Ω_t is the support of $\boldsymbol{p}$ at time t and A_t is the material region at time t, such that $A_0 = \Omega_0$. We conjecture that for generic initial conditions the following equality holds:

$$\Omega_t = \bigcup_{\tau=0}^{t} A_\tau.$$

The MP gauge. The impulse equation in this gauge was discovered by Maddocks & Pego. This form arises when deriving an unconstrained Hamiltonian form of the Euler equations. They indicate that this gauge might be useful in free boundary problems. In addition, in the framework developed by Maddocks & Pego they can also derive the impulse equation in the geometric gauge. We note that in the MP gauge the support of $\boldsymbol{p}$ is not compact for $t > 0$, even if the initial support is compact.

The EL gauge. This gauge has been introduced by E & Liu (1998) with the purpose of obtaining a stable finite difference scheme for the Navier–Stokes equations. They

https://doi.org/10.1017/S0022112099005170 Published online by Cambridge University Press

found that by using this gauge it is easier to obtain high-order projection methods for the Navier–Stokes equations on a non-staggered grid.

The geometric gauge. This is probably the most extensively studied impulse equation. In this gauge the impulse variable has an interesting geometrical interpretation. The following discussion is closely related to ideas developed in Sagdeev *et al* (1989), Buttke (1993), and Tur & Yanovsky (1993). We begin with the geometrical properties of the vorticity, which may be more familiar to the reader. The vorticity equation for incompressible flow is

$$\frac{\mathrm{D}\boldsymbol{\omega}}{\mathrm{D}t} = \boldsymbol{\omega}\cdot\nabla\boldsymbol{u}, \tag{2.21}$$

where $\mathrm{D}/\mathrm{D}t \equiv \partial/\partial t + \boldsymbol{u}\cdot\nabla$ is the material derivative. Now let $\boldsymbol{\ell}$ be a vector field associated with an infinitesimal line element of the fluid. The time evolution of $\boldsymbol{\ell}$ in an arbitrary incompressible flow is given by (Batchelor 1967, § 3.1)

$$\frac{\mathrm{D}\boldsymbol{\ell}}{\mathrm{D}t} = \boldsymbol{\ell}\cdot\nabla\boldsymbol{u}.$$

This equation is identical to the vorticity equation, and therefore, if we initialize $\boldsymbol{\ell}$ to be a vortex line, then the vortex lines evolve as fluid line elements, or, to use a popular expression, vortex lines are *frozen into the fluid*.

Next we consider a vector field $\boldsymbol{S}$ associated with oriented material surface elements of an incompressible fluid. Its evolution in an arbitrary divergence-free vector field $\boldsymbol{u}$ is given by

$$\frac{\partial\boldsymbol{S}}{\partial t} + \boldsymbol{u}\cdot\nabla\boldsymbol{S} = -(\nabla\boldsymbol{u})^{T}\boldsymbol{S}. \tag{2.22}$$

A derivation of this equation can be found in Batchelor (1967, § 3.1). If we compare this to the equation for the impulse density in the geometric gauge (2.11), we see that they are the same. Therefore it follows that the oriented surface (defined locally) associated with the impulse density (see figure 1 from Tur & Yanovsky 1993) must be frozen into the fluid.

Therefore we see that vortex lines are material lines, and impulse surfaces are material surfaces. Furthermore, a direct consequence of the equations of motion for $\boldsymbol{p}$ and $\boldsymbol{\omega}$ is

$$\frac{\mathrm{D}(\boldsymbol{p}\cdot\boldsymbol{\omega})}{\mathrm{D}t} = 0.$$

Because of the geometric interpretation of $\boldsymbol{p}$ and $\boldsymbol{\omega}$ in terms of surface and line elements, the geometric interpretation of this equation is merely conservation of volume elements of the fluid, i.e. incompressibility of the flow.

Next we shall give a plausibility argument that the vorticity will concentrate on tubes whereas the impulse density will concentrate on sheets. Let λ_1, λ_2, and λ_3 be the eigenvalues of $\nabla\boldsymbol{u}$. Since $\nabla\cdot\boldsymbol{u} = 0$ then it follows that

$$\lambda_1 + \lambda_2 + \lambda_3 = 0.$$

The vorticity will grow fastest when one of eigenvalues is a large positive number and the other two are negative. This means that the flow is stretching in one direction and compressing in the other two directions. This explains why vorticity tends to concentrate in thin tubes. On the other hand the impulse, in the geometric gauge, will grow fastest when one of the eigenvalues is a large negative number and the other two are positive, indicating that the flow is being stretched in two directions and compressed in the other one. Therefore, we expect that the impulse

https://doi.org/10.1017/S0022112099005170 Published online by Cambridge University Press

will concentrate in thin sheets. This interpretation along with (2.17) and numerical experiments suggest that the L^2 norm of $\boldsymbol{p}$ will increase monotonically in time when $\boldsymbol{p}$ is initially divergence-free. Chorin (1994) has proposed a similar conjecture for the L^1 norm.

In two space dimensions $\boldsymbol{u}$ and $\boldsymbol{\omega}$ are orthogonal to each other; there is no stretching term and (2.21) becomes

$$\frac{\partial \omega}{\partial t} + \boldsymbol{u} \cdot \nabla \omega = 0, \tag{2.23}$$

where $\boldsymbol{\omega} = (0, 0, \omega)^T$. Consequently, in two dimensions the vorticity is conserved along fluid paths. As is well known, one sees that the behaviour of the vorticity is dramatically different in two and three dimensions. However, the stretching term is present for the impulse equation, therefore we do not expect such dramatic differences between two and three dimensions.

We also mention that the impulse equation in this gauge has been given a physical interpretation in terms of magnetization by Buttke & Chorin (1993). Smereka (1996) also gives a similar physical interpretation using a slightly different gauge.

Exact solutions for the Geometric gauge. We present some exact results to show that the impulse can grow in time even for some simple steady flows. Consider the following exact solution of the two-dimensional Euler equations:

$$\omega = f(r) \quad \text{where} \quad r = \sqrt{x^2 + y^2},$$

then

$$\boldsymbol{u} = U(r)\widehat{\boldsymbol{u}}_\theta \quad \text{where} \quad U(r) = \frac{1}{r}\int_0^r f(s) s \mathrm{d}s,$$

where $\widehat{\boldsymbol{u}}_\theta$ is the unit vector in the θ-direction. An exact solution of the impulse equation is given by

$$\boldsymbol{p} = p_r \widehat{\boldsymbol{r}} + p_\theta \widehat{\boldsymbol{\theta}}$$

with

$$p_r = -U(r)U'(r)t, \quad \text{and} \quad p_\theta = U(r).$$

We see that for this steady flow the impulse grows linearly in time.

As a second example we take the 2π-periodic stationary solution of the two-dimensional Euler equations $\boldsymbol{u} = \boldsymbol{u}_s = (u, v)$ where

$$u(x, y) = \sin y \cos x,$$
$$v(x, y) = -\sin x \cos y.$$

Consider the impulse equation in the geometric gauge with initial data

$$\boldsymbol{p}(x, y, 0) = \boldsymbol{u}_s(x, y) + \nabla \psi \tag{2.24}$$

where

$$\psi = \sin x \cos y + \sin y \cos x.$$

It is clear that $\boldsymbol{u}$ is the divergence-free projection of $\boldsymbol{p}(x, y, 0)$. Using the exact solution for $\boldsymbol{u}$ in (2.11) we find

$$\frac{\partial p(\pi/2, \pi/2, t)}{\partial t} = p(\pi/2, \pi/2, t) \quad \text{and} \quad \frac{\partial q(\pi/2, \pi/2, t)}{\partial t} = -q(\pi/2, \pi/2, t),$$

where (p, q) are the two components of $\boldsymbol{p}$.

https://doi.org/10.1017/S0022112099005170 Published online by Cambridge University Press

Consequently,

$$p(\pi/2, \pi/2, t) = -\mathrm{e}^{t} \quad \text{and} \quad q(\pi/2, \pi/2, t) = -\mathrm{e}^{-t}. \tag{2.25}$$

Therefore, at the stagnation point the impulse grows exponentially fast. We expect this to be true in general.

2.2. *Hamiltonian formulations*

Maddocks & Pego (1995) showed that the impulse equation is a Hamiltonian system in Lagrangian variables in the geometric gauge and in the MP gauge. Oseledets (1989) deduced the Hamiltonian structure in Eulerian form in the geometric gauge.

The Hamiltonian formulation of Euler equations offers several potential advantages, that could be used both for theoretical and computational purposes. A Lagrangian description of the fluid can be obtained by a suitable discretization of the Hamiltonian. The equations of motion of the fluid particles will then be Hamilton's equations associated with the discrete Hamiltonian of the fluid. Such a formulation has the advantage that some integral of the motion will be preserved exactly (by the semi-discrete scheme). Such schemes (like vortex methods) have no numerical dissipation. Buttke (1993) exploited some of the properties offered by this formulation, and proposed a blob method for the numerical solution of the impulse equations in the geometric gauge.

Another possible advantage of this formulation is that the interaction of the fluid with other fields can be treated in a natural way, whenever the field can be described by a potential energy. The system is then described by the Hamiltonian of the fluid plus the Hamiltonian associated with the field. This approach has been considered by Recchioni & Russo (1998), who studied the interaction of a fluid with a membrane in two and three dimensions, both from an analytical and computational point of view, using the impulse equations in the geometric gauge. A similar problem has been considered by Cortez (1996), who studied also the effect of viscosity.

3. Numerical approach

Initially one might hope that the impulse formulation provides a better framework for the numerical solution of the Euler equations. In fact such an approach has been explored by several authors who used Lagrangian schemes based on the impulse formulation, see Buttke, Cortez, and Recchioni & Russo. In addition, some boundary conditions can be implemented in more natural way.

This approach suffers from a serious drawback, however. As we shall see the impulse variable can grow very fast and become concentrated. This causes the accuracy of schemes based on the impulse variables to degrade quickly. Nevertheless, it is possible to construct numerical methods for the impulse equation which mitigate this difficulty.

Finite difference schemes based on the impulse variables have been studied by E & Liu (1997). They show that the velocity-impulse formulation of the Euler equations is marginally ill-posed, and this has serious consequences for the stability properties of finite difference schemes based on this formulation.

We shall compare different schemes for the solution of the impulse equation with different gauges in two and three dimensions. We consider a domain $\Omega = [0, 2\pi]^d$ with periodic boundary conditions. In the schemes described below we use a discrete projection operator that is discretely divergence free with respect to centre differencing.

https://doi.org/10.1017/S0022112099005170 Published online by Cambridge University Press

3.1. *Numerical methods*

Method 1. The first scheme, denoted NAIVE2D, uses the $\boldsymbol{p}$ variable as the unknown field. The semi-discrete equations for $\boldsymbol{p}$ are

$$\frac{\partial P}{\partial t} = F \quad \text{and} \quad \frac{\partial Q}{\partial t} = H, \tag{3.1}$$

where (P, Q) is the discretization of the two components of $\boldsymbol{p}$ on a square grid with mesh size $2\pi/N$,

$$F = -(UD_xP + VD_yP + PD_xU + QD_xV),$$

and

$$H = -(UD_xQ + VD_yQ + PD_yU + QD_yV).$$

Here (U, V) is the discrete velocity field. D_x and D_y are centre-difference operators on the periodic grid. (U, V) is obtained from a discrete divergence-free projection of (P, Q) using Chorin's projection method.

For the convenience of the reader we briefly recall Chorin's method. We first define a discrete gradient, G, and a discrete divergence, D, as follows:

$$G\phi = (D_x\phi, D_y\phi)^T, \quad \text{and} \quad D \cdot (P, Q)^T = D_xP + D_yQ$$

The discrete form of (2.7) is

$$D \cdot G\phi = D \cdot (P, Q)^T$$

and the discrete divergence-free projection of $(P, Q)^T$ is

$$(U, V)^T = (P, Q)^T - G\phi \equiv \mathbf{P}_{\mathrm{N}}(P, Q)^T.$$

Equations (3.1) are discretized in time by a fourth-order Runge–Kutta scheme. With this choice of time discretization the centre-difference scheme is stable.

A result of this scheme is shown in figure 1. The initial conditions are given by (2.24). A 64×64 grid has been used, with a time step $\Delta t = 0.1$. This is a steady solution of the Euler equations, and therefore the vorticity should be constant in time. We see that the solution is no longer accurate at time $t = 1.6$. From the figure it is evident that $|\boldsymbol{p}|$ is concentrating and increasing near the hyperbolic points of the flow map causing loss of resolution of the numerical solution. This loss of resolution causes the numerical errors in the projection step. This causes errors in the velocity field.

E & Liu (1997) have also pointed out difficulties with NAIVE2D. They have shown that the impulse equation is only weakly well-posed. This can cause numerical difficulties. They were able to develop numerical methods to alleviate this problem. Below we also present methods which provide better numerical solutions to the impulse equation.

Method 2. A better scheme for the solution of the impulse equation is obtained by solving the Euler equations for $\boldsymbol{u}$ rather than taking the divergence-free projection of $\boldsymbol{p}$. The Euler and impulse equations are solved by discretizing the equations

$$\frac{\partial \boldsymbol{u}}{\partial t} = -\mathbf{P}(\boldsymbol{u} \cdot \nabla \boldsymbol{u}), \quad \frac{\partial \boldsymbol{p}}{\partial t} = -\boldsymbol{u} \cdot \nabla \boldsymbol{p} - (\nabla \boldsymbol{u})^T \boldsymbol{p}. \tag{3.2}$$

Equation (3.2) is discretized as

$$\frac{\partial}{\partial t}(U, V)^T = -\mathbf{P}_{\mathrm{N}}\left((U, V) \cdot G(U, V)^T\right). \tag{3.3}$$

https://doi.org/10.1017/S0022112099005170 Published online by Cambridge University Press

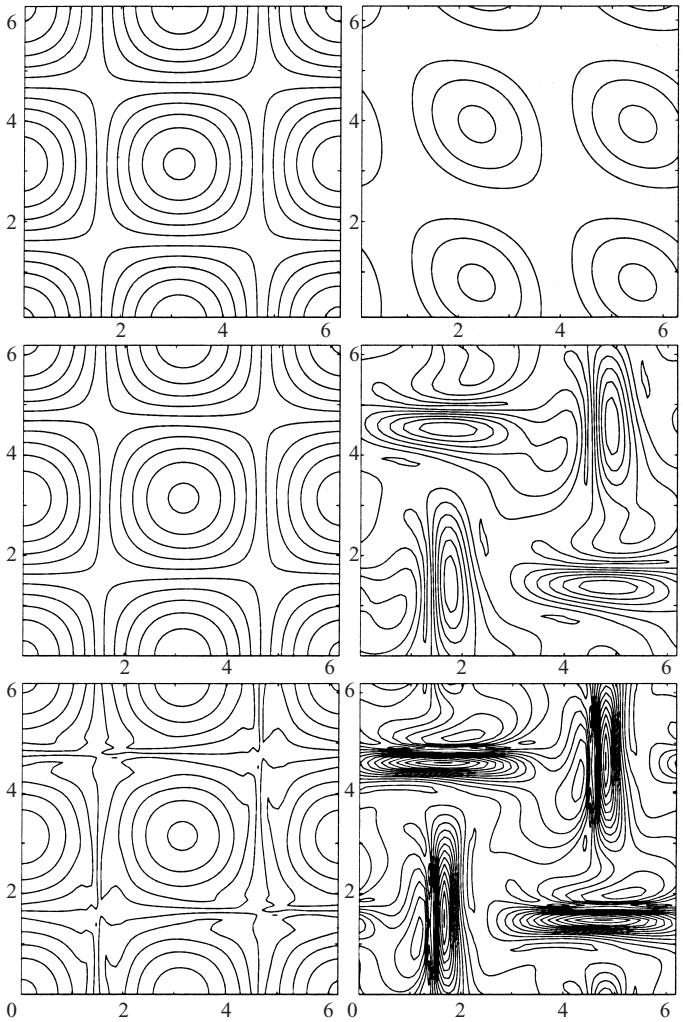


FIGURE 1. NAIVE2D results. The left-hand column shows contour plots of $|\omega|$ at t =0, 1.0, and 1.6 from top to bottom. The spacing between the contours is 0.4. The right-hand column shows the corresponding contour plots of $|\boldsymbol{p}|$. The spacing between the contours is 0.5.

Method 3. A slightly better scheme can be obtained by solving (3.2) together with the equation for ϕ. This has the advantage of computing a scalar field and appears to be more accurate. The semi-discrete equation for ϕ in the geometric gauge is given by

$$\frac{\partial \Phi}{\partial t} = -\tfrac{1}{2}(U^2 + V^2) - UD_x\Phi - VD_y\Phi + \mathscr{P}. \tag{3.4}$$

The pressure is computed by solving the Poisson equation

$$-\Delta\mathscr{P} = \nabla \cdot (\boldsymbol{u} \cdot \nabla \boldsymbol{u}).$$

We note that this is an intermediate step in the projection method. Equation (3.4), together with (3.3), is discretized in time by a fourth-order Runge–Kutta scheme. The

https://doi.org/10.1017/S0022112099005170 Published online by Cambridge University Press

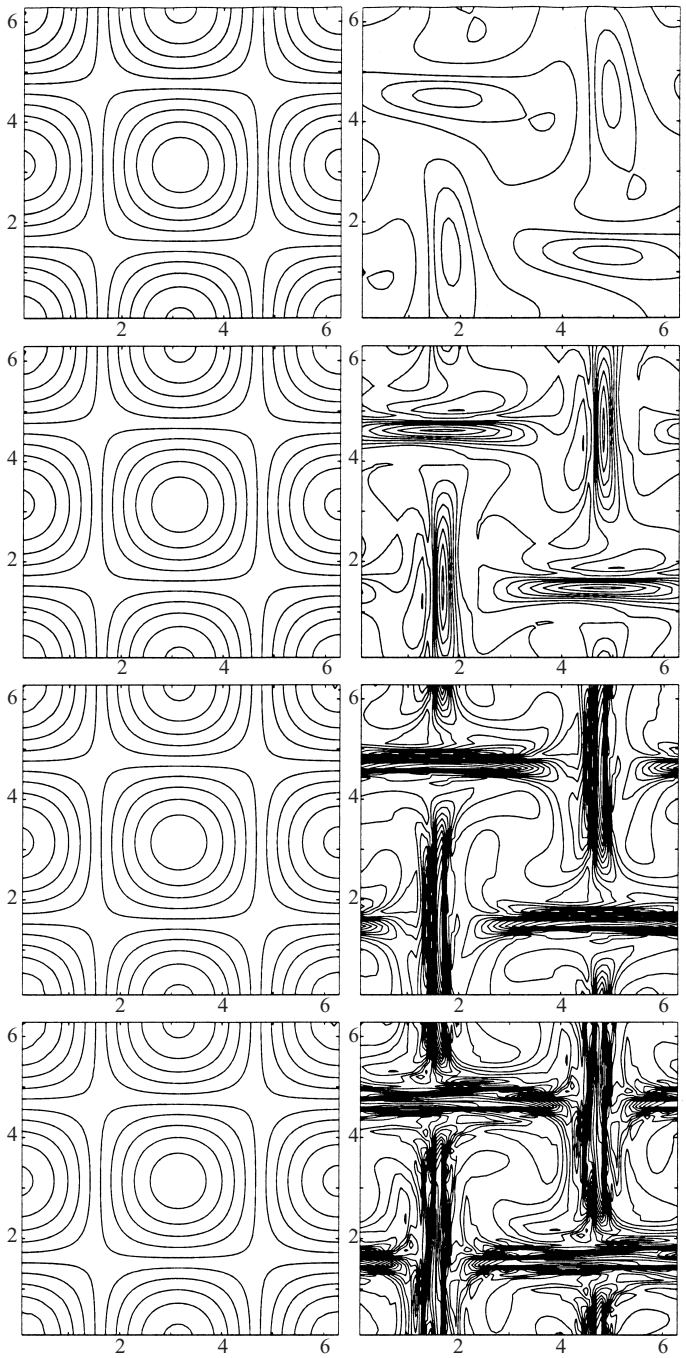


FIGURE 2. PHI2D results for same initial condition as in figure 1. The left-hand column shows contour plots of $|\boldsymbol{\omega}|$ at $t = 1$, 2, 3, and 4 from top to bottom. The spacing between the contours is 0.4. The right-hand column shows the corresponding contour plots of $|\boldsymbol{p}|$. The spacing between the contours is 1.

https://doi.org/10.1017/S0022112099005170 Published online by Cambridge University Press

	Relative error (%)					
	64×64 grid			128×128 grid		
Time	L^1	L^2	L^∞	L^1	L^2	L^∞
1.0	0.99	0.46	0.56	0.40	0.15	0.16
2.0	6.42	2.61	4.45	4.59	0.48	0.71
3.0	31.1	11.1	20.7	6.86	2.26	4.81
4.0	70.0	31.2	53.5	32.8	8.40	21.8

TABLE 1. Error in the impulse computed by differencing relative to figure 2.

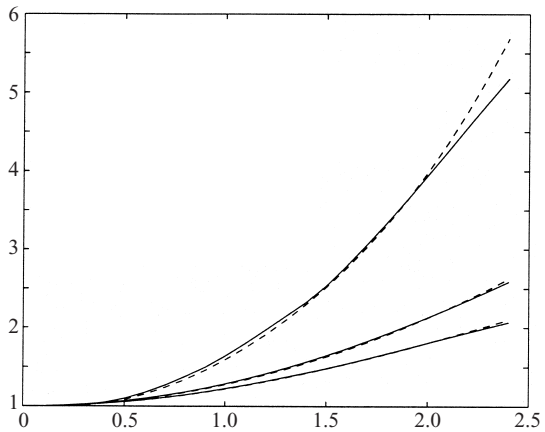


FIGURE 3. Comparison between LAG2D (dashed curves) and PHI2D (solid curves). The upper pair of curves are the L^∞ norms, the middle pair is the L^2 norm, and the lower pair is the L^1 norm.

impulse is reconstructed on the grid by

$$P = U + D_x\Phi, \quad Q = V + D_y\Phi.$$

We shall call this scheme PHI2D.

Figure 2 shows the results of the calculations with the same initial conditions used in figure 1. Here we see that $\boldsymbol{\omega}$ is much better behaved and we can now compute longer in time. In this formulation the loss of resolution of $\boldsymbol{p}$ does not pollute the calculation of the velocity field.

The error in the computation of the impulse field is summarized in table 1. The error corresponding to a $N \times N$ grid is obtained by comparing the solution to the one obtained on a $2N \times 2N$ grid. The relative error in the vorticity for a 128×128 grid is less than 1% both in the L^1 and L^2 norms.

Method 4. A better accuracy is obtained by integrating directly the impulse equations in Lagrangian form. The equations are integrated along the particle trajectories, by solving the equations

$$\frac{\mathrm{d}\tilde{\boldsymbol{x}}}{\mathrm{d}t} = \tilde{\boldsymbol{u}}, \quad \frac{\mathrm{d}\tilde{\boldsymbol{p}}}{\mathrm{d}t} = -(\nabla\tilde{\boldsymbol{u}})^T\tilde{\boldsymbol{p}}. \tag{3.5}$$

The velocity at each particle location is computed by linear interpolation of the velocity previously computed on the grid by differencing, and then interpolated on

https://doi.org/10.1017/S0022112099005170 Published online by Cambridge University Press

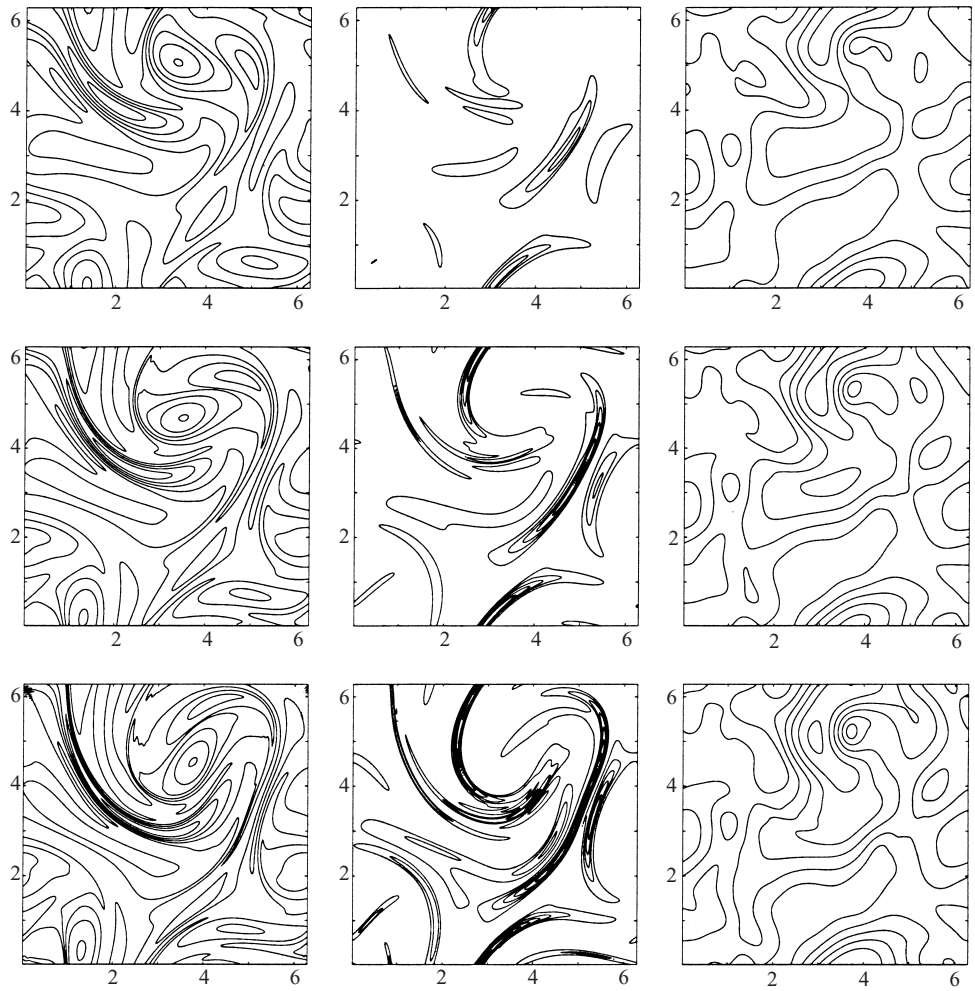


FIGURE 4. Phi2D results. The left-hand column shows contours of ω at times $t = 15$, 21, and 27 from top to bottom, the contours are separated by 0.1 The middle column shows contours of $|\boldsymbol{p}|$ at times $t = 15$, 21, and 27 from top to bottom, in the geometric gauge; the contours are separated by 0.5. The right-hand column shows the contours of $|\boldsymbol{p}|$ in the EL gauge; the contours are separated by 0.1.

the particle. Such a scheme is not a genuine Lagrangian scheme, but it is rather an integration along fluid lines. A similar approach is often used in Eulerian fluid dynamics codes, when one is interested in computing particle trajectories. We shall call the scheme LAG2D.

Equations (3.5) do not contain a gradient in $\boldsymbol{p}$, and therefore they give a more accurate description of the evolution of the impulse. The disadvantage of a Lagrangian approach is that the field is computed on particle locations, and it is difficult to interpolate the scattered data on a regular grid. An advantage of the Lagrangian approach is that it provides a very accurate way to compute L^p norms. We use this feature as a diagnostic tool.

The evolution of the norms is computed and shown in figure 3 compared with the results from PHI2D. At the initial time the test particles are uniformly distributed

https://doi.org/10.1017/S0022112099005170 Published online by Cambridge University Press

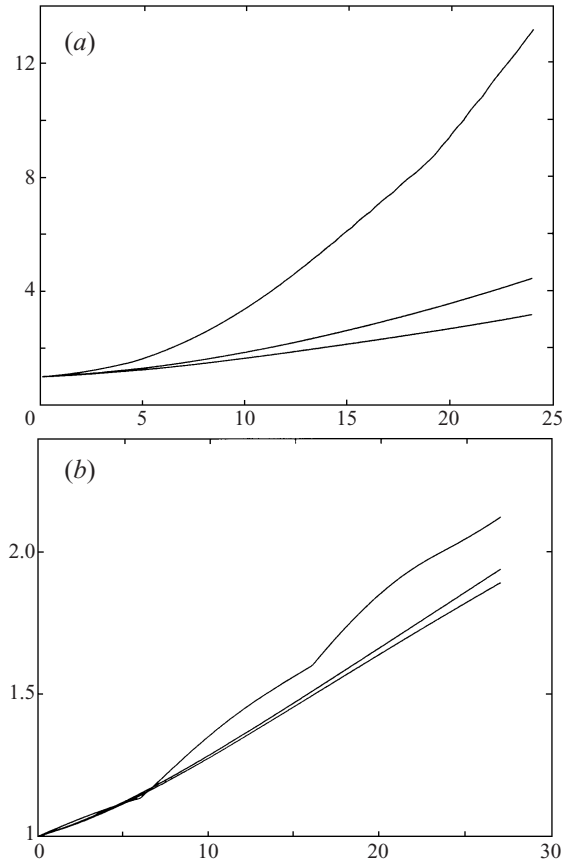


FIGURE 5. The L^∞, L^2, and L^1 norms are shown for the results in figure 4, corresponding to the geometric gauge (*a*) and EL gauge (*b*). In each plot, the upper curve is the L^∞ norm, the middle one is the L^2 norm, and the lower curve is the L^1 norm. The norms have been normalized to be equal to 1 at $t = 0$.

in $[0, 2\pi]^2$. A Van der Corput sequence is used to obtain a low-discrepancy uniform distribution. The norms have been normalized with respect to the initial conditions.

The two numerical solutions are in good agreement up to about time $t = 2$. For later times, the numerical solution for ϕ is not well-resolved and the region of large gradients of ϕ is not accurately computed. The main reason for the loss of accuracy is the presence of a convective term in the equation for ϕ, which involves the computation of $\nabla\phi$.

4. Numerical results

In the following numerical calculations we shall use PHI2D. We shall use a straightforward extension of this method for three-dimensional flows.

4.1. *Two space dimensions*

We use the following initial conditions to examine an unsteady two-dimensional flow:

$$\boldsymbol{p} = \sum_{i,j=1}^{N} \widehat{\boldsymbol{p}}_{ij} \cos(ix + jy + \theta_{ij}), \tag{4.1}$$

https://doi.org/10.1017/S0022112099005170 Published online by Cambridge University Press

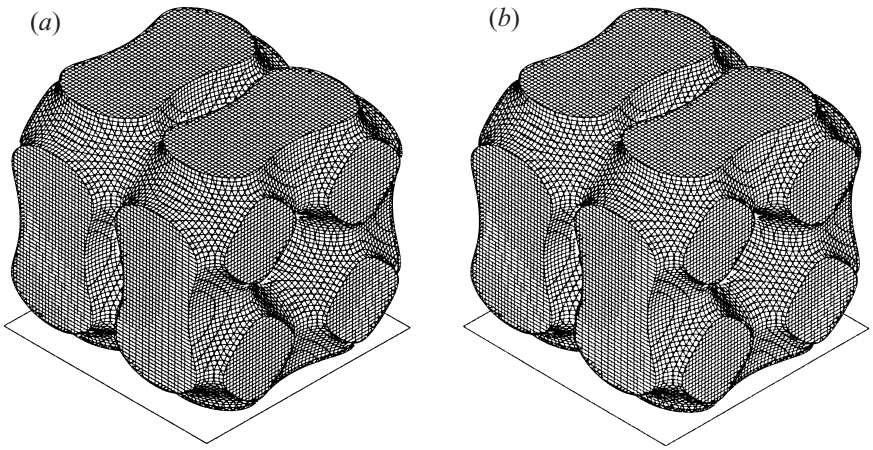


FIGURE 6. Beltrami flow: (*a*) the contours of $|\boldsymbol{\omega}(\boldsymbol{x},t)| = 0.55||\boldsymbol{\omega}(\cdot,t)||_\infty$ at $t = 0$; (*b*) the contours of $|\boldsymbol{\omega}(\boldsymbol{x},t)| = 0.55||\boldsymbol{\omega}(\cdot,t)||_\infty$ at $t = 2$.

where

$$\widehat{\boldsymbol{p}}_{ij} = \frac{1}{(i^2+j^2)^{1/2}}(\cos(\alpha_{ij})\boldsymbol{e}_x + \sin(\alpha_{ij})\boldsymbol{e}_y);$$

α_{ij} and θ_{ij} are random variables with a uniform distribution in $[0, 2\pi]$. We compute the vorticity and the impulse in two different gauges, namely the geometric gauge and the EL gauge. The results are shown on figure 4 for $N = 3$. In this computation we use a 256×256 mesh with time step of 0.1. In the geometric gauge the general feature is that the impulse variable concentrates in 'sheets'. The concentration of impulse is evident also by looking at the norms. The L^∞ norm, in fact, increases much more than the other norms (figure 5). A completely different behaviour is observed in the EL gauge. In this case the impulse does not increase dramatically, and no concentration is observed. The different norms increase at a similar rate.

It is evident from figures 2 and 4 that the impulse (in the geometric gauge) tends to concentrate in sheets corresponding to regions of large shear. Such behaviour will appear also in three-dimensional flows.

4.2. *Three space dimensions*

In this section we present results of PHI3D which is three-dimensional version of PHI2D. We consider three cases. The first one is a Beltrami flow, the second represents two interlocking vortex rings and the third is the interaction of two vortex tubes. In the last two cases we will see that the $\boldsymbol{p}$ will concentrate on sheets whereas the vorticity concentrates on tubes. The computational domain is a cube with sides of length 2π. We have 64 mesh points on a side and we use a time step of 0.05.

4.2.1. *Beltrami flows*

Beltrami flows are stationary solutions of the incompressible Euler equations in which $\boldsymbol{\omega}$ is parallel to $\boldsymbol{u}$. The following choice of $\boldsymbol{p}$ yields such a flow:

$$\boldsymbol{p}(\boldsymbol{x},0) = (p_x, p_y, p_z)$$

with

$$p_x = \sin x \cos y + \sqrt{2}\sin z \sin y,$$

https://doi.org/10.1017/S0022112099005170 Published online by Cambridge University Press

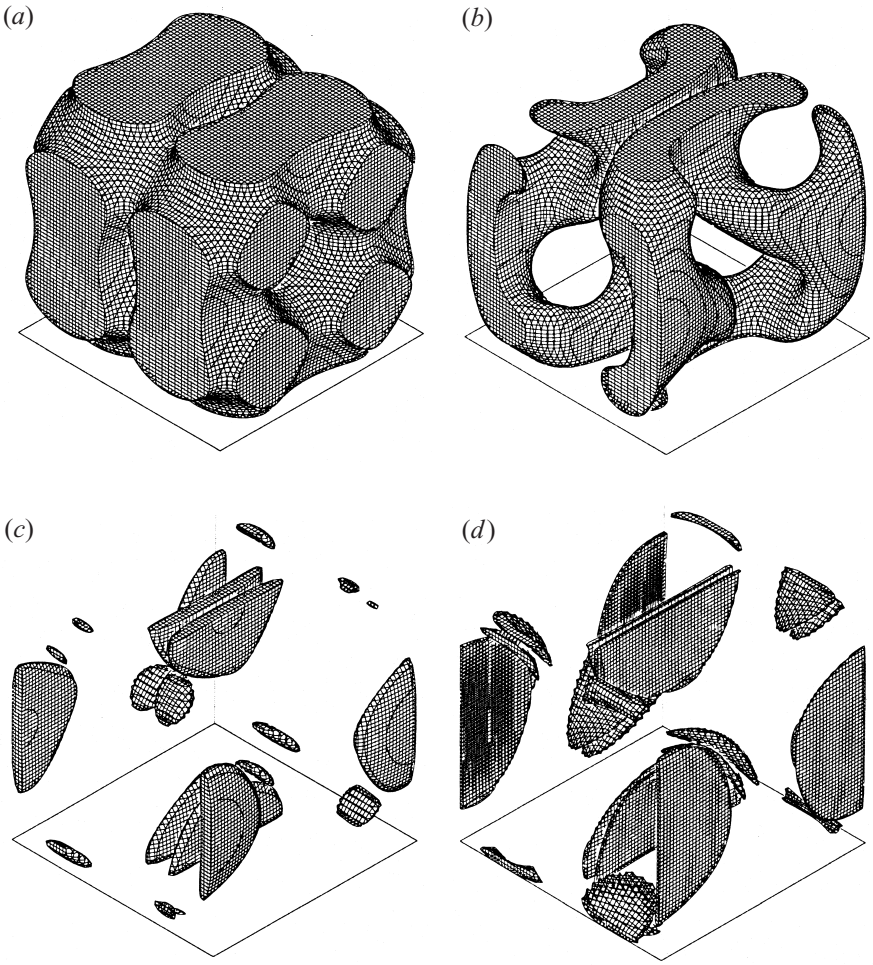


FIGURE 7. Beltrami flow: the contours of $|\boldsymbol{p}(\boldsymbol{x},t)| = 0.55||\boldsymbol{p}(\cdot,t)||_\infty$ at (*a*) $t = 0$, (*b*) $t = 0.5$, (*c*) $t = 1$ and (*d*) $t = 2$.

$$p_y = -\cos x \sin y + \cos z \sin y,$$

$$p_z = \sqrt{2}\sin x \sin y - \sin z \cos y.$$

The results are shown in figures 6 and 7. Figure 6 shows that the vorticity is constant in time as expected whereas figure 7 shows the impulse density concentrating on sheets. The regions of large concentration of impulse correspond to the region where the negative eigenvalue of the matrix $\nabla \boldsymbol{u}$ is largest (in absolute value).

4.2.2. *Interlocking vortex rings*

Here we take the following initial condition for the impulse density:

$$\boldsymbol{p}(\boldsymbol{x},0) = (p_x, p_y, p_z)$$

with

$$p_x = \tfrac{1}{2}\exp\left[-4(x-\pi)^2\right]\left(\operatorname{erf}(a_{zy}) + 1\right), \quad p_y = 0,$$

https://doi.org/10.1017/S0022112099005170 Published online by Cambridge University Press

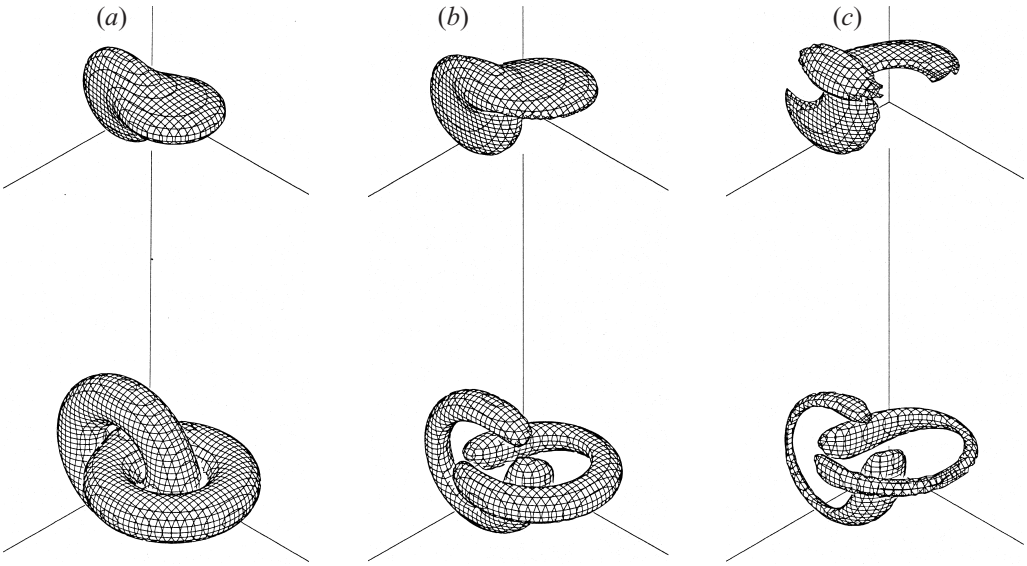


FIGURE 8. Interlocking vortex rings: the figures on the bottom show the contours of $|\boldsymbol{\omega}(\boldsymbol{x},t)| = 0.55||\boldsymbol{\omega}(\cdot,t)||_\infty$, and the figures on the top the contours of $|\boldsymbol{p}(\boldsymbol{x},t)| = 0.55||\boldsymbol{p}(\cdot,t)||_\infty$ at (*a*) $t = 0$, (*b*) $t = 1.8$, (*c*) $t = 3.3$.

and

$$p_z = \tfrac{1}{2}\exp\left[-4(z-\pi)^2\right]\left(\operatorname{erf}(a_{xy})+1\right),$$

where

$$a_{zy} = 2\left(1-\sqrt{(y-\pi+\tfrac{1}{2})^2+(z-\pi)^2}\right)$$

and

$$a_{xy} = 2\left(1-\sqrt{(y-\pi-\tfrac{1}{2})^2+(x-\pi)^2}\right).$$

This corresponds to a vorticity distribution consistent with two interacting vortex rings. The numerical results are shown in figure 8 which shows the isosurfaces $|\boldsymbol{\omega}(\boldsymbol{x},t)| = 0.55||\boldsymbol{\omega}(\cdot,t)||_\infty$ and $|\boldsymbol{p}(\boldsymbol{x},t)| = 0.55||\boldsymbol{p}(\cdot,t)||_\infty$ at different times.

Note that the apparent breaking of the topology of the vortex ring is only an effect of the way the numerical results are visualized. It is well known, in fact, that vortex ring breaking is not possible with the Euler equation.

In the numerical simulations we see that the vorticity becomes concentrated in tubes and the impulse is concentrating on sheets. Figure 9 shows that for both $\boldsymbol{\omega}$ and $\boldsymbol{p}$ the L^∞ norm increases faster than the L^1 norm. This is consistent with the notion that the vorticity and impulse density are becoming more concentrated.

4.2.3. *Two vortex tubes*

We first define

$$r_{xy} = (x^2+y^2)^{1/2}, \quad r_{yz} = (y^2+z^2)^{1/2}$$

and

$$C(r) = \begin{cases} 1-10r^3+15r^4-6r^5, & 0<r<1 \\ 0, & r \geqslant 1. \end{cases}$$

https://doi.org/10.1017/S0022112099005170 Published online by Cambridge University Press

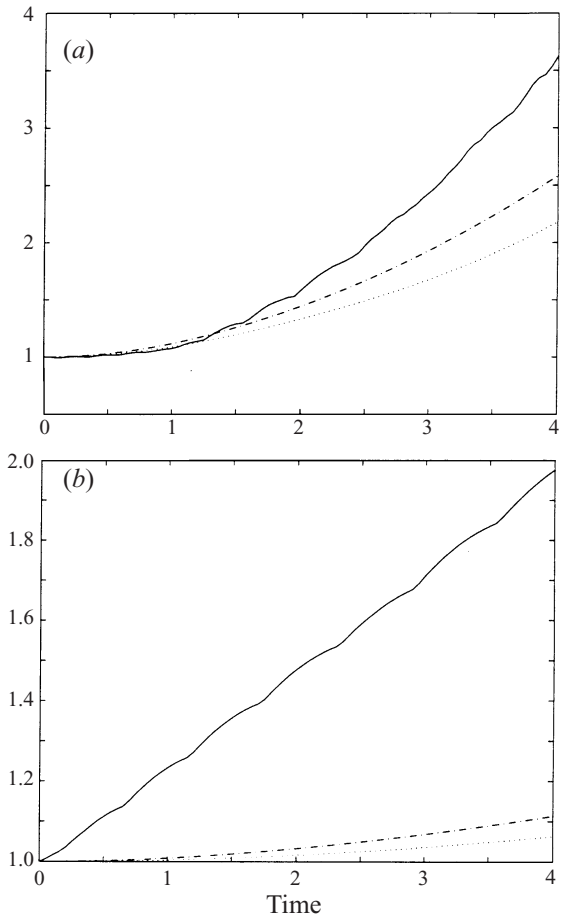


FIGURE 9. The L^1 (dotted curve), L^2 (dot-dashed), and L^∞ (solid) norms are presented for the interlocking vortex rings: (*a*) for $\boldsymbol{\omega}$ and (*b*) for $\boldsymbol{p}$.

Next we consider

$$\boldsymbol{p}_z = \begin{pmatrix} yC(r_{xy}/2) \\ -xC(r_{xy}/2) \\ 0 \end{pmatrix} \quad \text{and} \quad \boldsymbol{p}_x = \begin{pmatrix} 0 \\ zC(r_{yz}/2) \\ -yC(r_{yz}/2) \end{pmatrix}.$$

One can see by taking the curl of $\boldsymbol{p}_z$ that it corresponds to a vortex tube centred on the z-axis. The vorticity is in the z-direction and it has a cross-section given by $C(r_{xy})$. On the other hand $\boldsymbol{p}_x$ corresponds to vortex tube centred on the x-axis with vorticity in the z-direction with a cross-section given by $C(r_{yz})$.

For initial conditions we use

$$\boldsymbol{p}(\boldsymbol{x}, 0) = \boldsymbol{p}_z + \tfrac{1}{2}\boldsymbol{p}_x. \tag{4.2}$$

The results of our numerical computations are shown in figures 10(*a–d*). In figure 10(*a*) only one vortex tube is shown because the other one is too weak to be seen. However, as time progresses the vorticity in the other tube starts to grow because of the stretching effects. At later stages the vortex tube in the z-direction becomes concentrated in an undulating tube whereas the vortex tube in the x-direction seems

https://doi.org/10.1017/S0022112099005170 Published online by Cambridge University Press

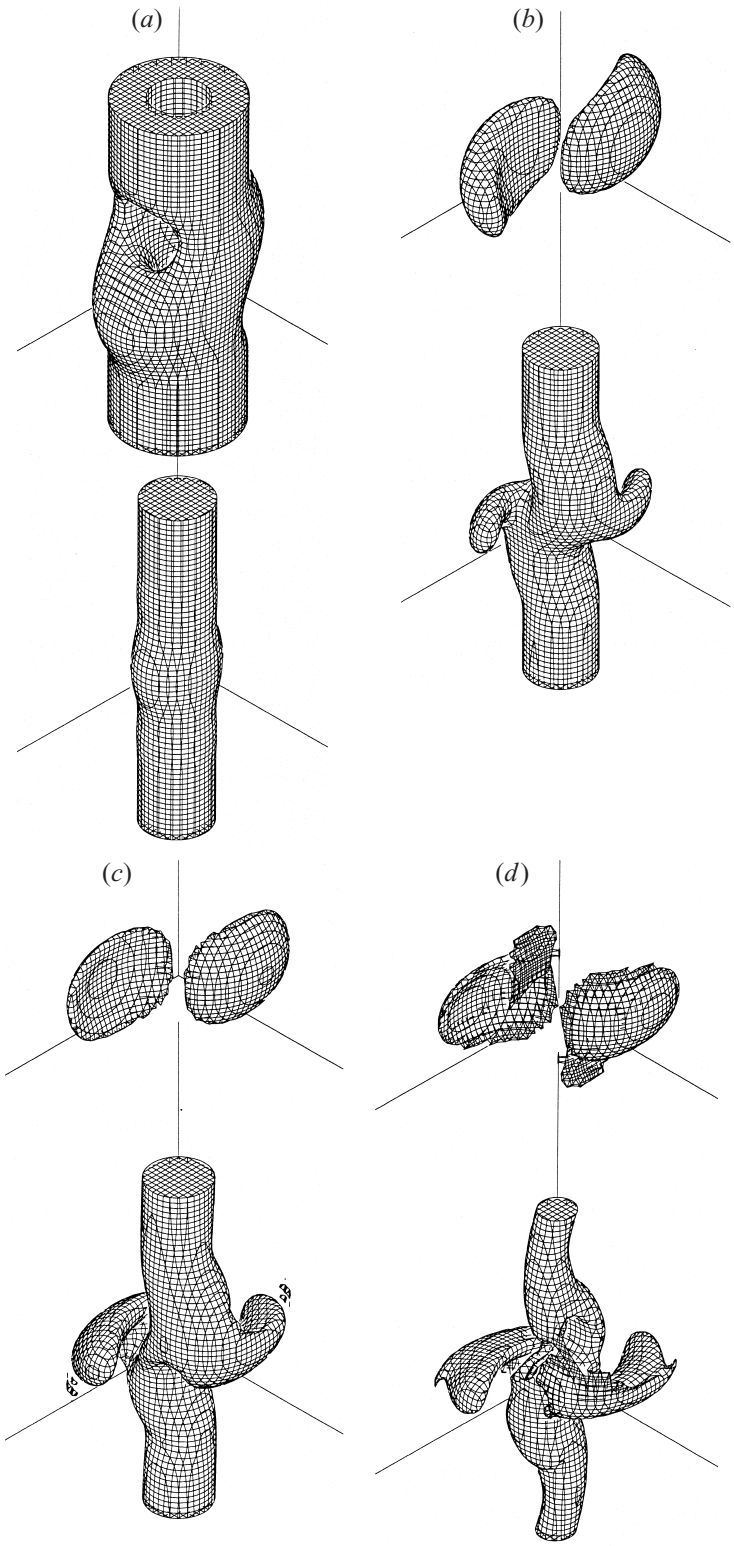


FIGURE 10. Vortex tubes: the figures on the bottom show the contours of $|\boldsymbol{\omega}(\boldsymbol{x},t)| = 0.55||\boldsymbol{\omega}(\cdot,t)||_\infty$; the figures on the top show the contours of $|\boldsymbol{p}(\boldsymbol{x},t)| = 0.55||\boldsymbol{p}(\cdot,t)||_\infty$. (*a*) $t = 0$, (*b*) $t = 1.25$, (*c*) $t = 2.75$, (*d*) $t = 4.0$.

https://doi.org/10.1017/S0022112099005170 Published online by Cambridge University Press

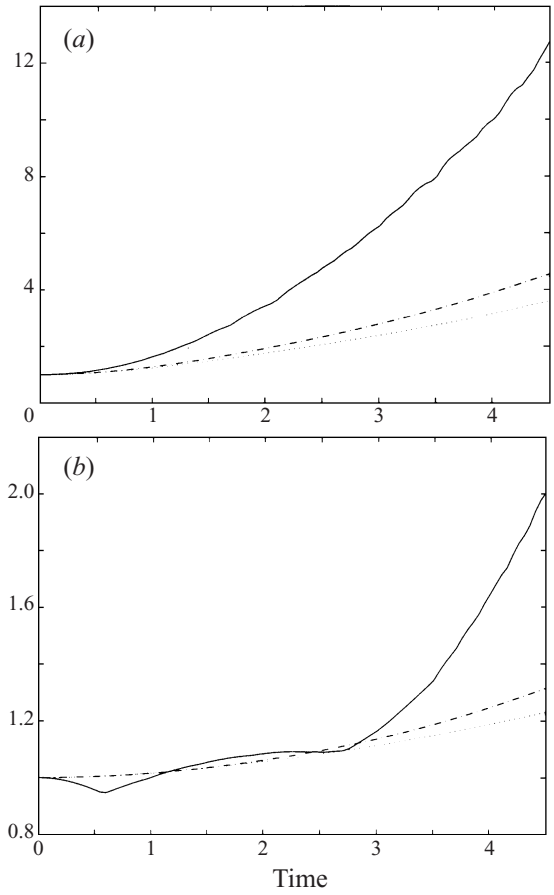


FIGURE 11. The L^1 (dotted curve), L^2 (dot-dashed), and L^∞ (solid) norms are presented for the vortex tubes: (*a*) for $\boldsymbol{p}$ and (*b*) for $\boldsymbol{\omega}$.

to concentrate on sheets. On the other hand the impulse quickly concentrates on sheets. Figure 11 presents the L^1, L^2, and L^∞ norms of both $\boldsymbol{\omega}$ and $\boldsymbol{p}$. They have been normalized so that they are initially equal to 1. For both $\boldsymbol{\omega}$ and $\boldsymbol{p}$ we see that the L^∞ norm is increasing faster than the L^1 norm, which is consistent with the notion that both variables are concentrating. It is interesting to notice that the L^∞ norm of $\boldsymbol{p}$ grows much faster than that of $\boldsymbol{\omega}$.

5. Summary

We have investigated various impulse formulations of the incompressible Euler equations. In particular we compute numerical solutions in the geometric gauge (this is the most common impulse equation). We observe that, because of the stretching term, the impulse variable is not convenient for computation. We developed alternative methods for the numerical solution of the impulse equations. We observe that the impulse variable tends to concentrate on sheets in two and three dimensions. It is interesting that the impulse variable behaves in similar fashion in both two and three dimensions unlike the vorticity variable. We also note that the impulse variable and the vorticity variable concentrate in different regions of the fluid. This indicates that

https://doi.org/10.1017/S0022112099005170 Published online by Cambridge University Press

the regions of high vorticity are not necessarily the most 'active' regions of the fluid. It also suggests that the impulse variable may be an interesting diagnostic tool for studying fluid flows.

The authors thank Robert Krasny for helpful discussions. This work was supported, in part, by the National Science Foundation through a Mathematical Sciences Career grant (Grant No DMS-9625190), and in part by CNR-NSF joint grant (CNR contract N.96.00181.CT01).

REFERENCES

Batchelor, G. K. 1967 *An Introduction to Fluid Dynamics*. Cambridge University Press.

Buttke, T. F. 1993 Velicity methods: Lagrangian numerical methods which preserve the Hamiltonian structure of incompressible fluid flow. In *Vortex Flows and Related Numerical Methods* (ed. J. T. Beale, G. H. Cottet & S. Huberson). Kluwer.

Buttke, T. F. & Chorin, A. J. 1993 Turbulence calculations in magnetization variables. *Appl. Numer. Maths* **12**, 47.

Chefranov, S. G. 1987 Dynamics of point-vortex dipoles and spontaneous singularities in three dimensional turbulent flows. *Sov. Phys. JETP* **66**, 85.

Chen, M. 1996 The velicity formulation of the Euler equation and the symplectic integration. PhD dissertation, New York University.

Chorin, A. J. 1994 Vortex phase transitions in $2\frac{1}{2}$ dimensions. *J. Statist. Phys* **76**, 835.

Cortez, R. 1996 An impulse-based approximation of fluid motion due to boundary forces. *J. Comput. Phys.* **123**, 341.

E, W. & Liu, J. G. 1997 Finite difference schemes for incompressible flows in the velocity-impulse density formulation. *J. Comput. Phys.* **130**, 67.

E, W. & Liu, J. G. 1998 Gauge methods for viscous incompressible flows. *J. Comput. Phys.* (submitted for publication).

Kuz'min, G. A. 1983 Ideal incompressible hydrodynamics in terms of the vortex momentum density. *Phys. Lett.* **96A**, 88.

Maddocks, J. H. & Pego, R. L. 1995 An unconstrained Hamiltonian formulation for incompressible fluid flow. *Commun. Math. Phys.* **170**, 207.

Oseledets, V. I. 1989 On a new way of writing the Navier–Stokes equation: The Hamiltonian formalism. *Russ. Math. Surveys* **44**, 210.

Recchioni, C. & Russo, M. G. 1998 Hamilton-based numerical methods for fluid-membrane interaction in 2d and 3d. *SIAM J. Sci. Comput.* **19**, 861–892.

Roberts, P. H. 1972 A Hamiltonian theory for weakly interacting vortices. *Mathematica* **19**, 169.

Sagdeev, R. Z., Moiseev, S. S., Tur, A. V. & Yanovsky, V. V. 1986 Problems of the theory of string turbulence and topological solitons. In *Nonlinear Phenomena in Plasma Physics and Hydrodynamics* (ed. R. Z. Sagdeev). Mir Publishers, Moscow.

Smereka, P. 1996 A Vlasov description of the Euler equation. *Nonlinearity* **9**, 1361.

Tur, A. V. & Yanovsky, V. V. 1993 Invariants in dissipationless hydrodynamic media. *J. Fluid. Mech.* **248**, 67.

https://doi.org/10.1017/S0022112099005170 Published online by Cambridge University Press